Received: 11 August 2022 | Revised: 31 January 2023 | Accepted: 13 February 2023

DOI: 10.1002/cyto.a.24723

ORIGINAL ARTICLE

ISAC CYTOMETRY Journal of Quantitative Cell Science PART A

Label-free multiphoton imaging flow cytometry

Ryo Kinegawa[1] | Julia Gala de Pablo[1] | Yi Wang[2] | Kotaro Hiramatsu[1,3,4] | Keisuke Goda[1,5,6,7]

[1]Department of Chemistry, The University of Tokyo, Tokyo, Japan

[2]Department of Chemistry, Renmin University of China, Beijing, China

[3]Research Centre for Spectrochemistry, The University of Tokyo, Tokyo, Japan

[4]PRESTO, Japan Science and Technology Agency, Saitama, Japan

[5]Institute of Technological Sciences, Wuhan University, Hubei, China

[6]Department of Bioengineering, University of California, Los Angeles, California, USA

[7]CYBO, Inc., Tokyo, Japan

Correspondence
Kotaro Hiramatsu, Department of Chemistry, The University of Tokyo, Tokyo 113-0033, Japan.
Email: hiramatsu@chem.s.u-tokyo.ac.jp

Funding information
JST PRESTO, Grant/Award Number: JPMJPR1878; JST FOREST, Grant/Award Number: JPMJFR216R; JSPS Gran-in-Aid for Scientific Research (B), Grant/Award Number: 22H02029; JSPS Grant-in-Aid for Young Scientists, Grant/Award Number: 20K15227; JSPS Core-to-Core Program; White Rock Foundation; Research Foundation for Opto-Science and Technology; JSPS Fellowship, Grant/Award Number: 19F19805

Abstract

Label-free imaging flow cytometry is a powerful tool for biological and medical research as it overcomes technical challenges in conventional fluorescence-based imaging flow cytometry that predominantly relies on fluorescent labeling. To date, two distinct types of label-free imaging flow cytometry have been developed, namely optofluidic time-stretch quantitative phase imaging flow cytometry and stimulated Raman scattering (SRS) imaging flow cytometry. Unfortunately, these two methods are incapable of probing some important molecules such as starch and collagen. Here, we present another type of label-free imaging flow cytometry, namely multiphoton imaging flow cytometry, for visualizing starch and collagen in live cells with high throughput. Our multiphoton imaging flow cytometer is based on nonlinear optical imaging whose image contrast is provided by two optical nonlinear effects: four-wave mixing (FWM) and second-harmonic generation (SHG). It is composed of a microfluidic chip with an acoustic focuser, a lab-made laser scanning SHG-FWM microscope, and a high-speed image acquisition circuit to simultaneously acquire FWM and SHG images of flowing cells. As a result, it acquires FWM and SHG images (100 × 100 pixels) with a spatial resolution of 500 nm and a field of view of 50 μm × 50 μm at a high event rate of four to five events per second, corresponding to a high throughput of 560–700 kb/s, where the event is defined by the passage of a cell or a cell-like particle. To show the utility of our multiphoton imaging flow cytometer, we used it to characterize *Chromochloris zofingiensis* (NIES-2175), a unicellular green alga that has recently attracted attention from the industrial sector for its ability to efficiently produce valuable materials for bioplastics, food, and biofuel. Our statistical image analysis found that starch was distributed at the center of the cells at the early cell cycle stage and became delocalized at the later stage. Multiphoton imaging flow cytometry is expected to be an effective tool for statistical high-content studies of biological functions and optimizing the evolution of highly productive cell strains.

KEYWORDS
imaging flow cytometry, microalgae, Muriella, nonlinear optics, second harmonic generation

1 | INTRODUCTION

Label-free imaging flow cytometry is a powerful tool for biological and medical research [1–5]. It overcomes technical challenges in conventional fluorescence-based imaging flow cytometry [6–14] that predominantly relies on labeling with fluorescent probes, such as their non-specific binding, low quantitative performance, and potential perturbation to the function of small molecules including metabolites and difficulties in labeling intracellular molecules [15, 16]. To date, two distinct types of label-free imaging flow cytometry have been developed. First, Lei et al. and Lau et al. demonstrated optofluidic time-stretch quantitative phase imaging flow cytometry which acquires quantitative phase images of numerous single cells at a high event rate of more than 10,000 events per second (eps) [1, 13]. This method enabled large-scale analysis and classification of numerous single cells with computational techniques such as machine learning and compressive sensing. Second, Suzuki et al. demonstrated stimulated Raman scattering (SRS) imaging flow cytometry which provides the ability to obtain chemical images of single cells based on molecular vibrations at a high event rate of up to 140 eps [2]. This method allowed the SRS-based visualization of paramylon, chlorophyll, and lipids within microalgal cells and the marker-free differentiation of cancer cells from blood cells without the need for fluorescent probes.

Despite those efforts, characterizing the full spectrum of complex biological systems in a label-free manner is still challenging due to the limited information obtained through these methods. Specifically, optofluidic time-stretch quantitative phase imaging does not provide chemical specificity and is, hence, unable to evaluate the chemical content of cells while providing their three-dimensional morphological content. On the other hand, SRS imaging flow cytometry can offer chemical specificity, but its chemical imaging ability is limited by the small cross-section of Raman scattering of biomolecules (10–30 cm^2/sr) [17] and the narrow bandwidth of SRS (normally constrained to the high-wavenumber region of 2800–3200 cm^{-1}) [2] which arises from the limited number of available laser sources. While the combination of label-free imaging and machine learning has enriched the biological interpretation of the acquired images, increasing the chemical information at the raw data level is essential to take full advantage of the capability of label-free imaging flow cytometry. Specifically, label-free imaging flow cytometry of some important molecules, such as starch and collagen, remains challenging.

In this paper, we present another type of label-free imaging flow cytometry, namely multiphoton imaging flow cytometry, for visualizing starch and collagen in live cells with high throughput. Our multiphoton imaging flow cytometer is based on nonlinear optical imaging whose image contrast is provided by two optical nonlinear effects: four-wave mixing (FWM) and second-harmonic generation (SHG). FWM is an effect arising from the third-order optical susceptibility of intracellular molecules and has been used for label-free imaging of cytoplasm with high contrast and spatial resolution [18, 19], whereas SHG is an effect arising from the second-order optical susceptibility of the molecules and has been used to visualize collagen [20], starch [21], and other non-centrosymmetric materials [22] in a label-free manner. The multiphoton imaging flow cytometer is composed of a microfluidic system, a SHG-FWM microscope with a raster-scanned focused beam, and a high-speed image acquisition circuit to simultaneously acquire FWM and SHG images of flowing cells. We employed the raster-scan arrangement over a wide-field or light-sheet arrangement [23–25] because the generation of the FWM and SHG signals is significantly enhanced under tightly focused light fields due to its nonlinear process. As a result, it acquires FWM and SHG images (100 × 100 pixels) with a 14-bit depth, a spatial resolution of 500 nm, and a field of view of 50 μm × 50 μm at a high event rate of 4–5 eps, corresponding to a high throughput of 560–700 kb/s [26].

To show the utility of our multiphoton imaging flow cytometer, we used it to characterize *Chromochloris zofingiensis* (NIES-2175), a unicellular green alga that has recently attracted attention from the industrial sector for its ability to efficiently produce valuable materials for bioplastics [27, 28], food [22, 29], and biofuel [30]. Currently, there is a high demand for optimizing the culture conditions of *C. zofingiensis* cells to improve their starch production efficiency. Traditionally, accumulated starch within *C. zofingiensis* cells is evaluated by Lugol staining [31] or colorimetry [32], but they require cell fixation, costly consumables, and time-consuming protocols. Moreover, colorimetry measures the amount of accumulated starch in a bulk manner in the units of starch weight per unit biomass and hence loses information related to cellular heterogeneity which is essential to understand cellular metabolism at the single-cell level. Our multiphoton imaging flow cytometer addressed this predicament by characterizing cell size, the amount of intracellular starch, and the spatial distribution of intracellular starch in a label-free manner. As a proof-of-principle demonstration, we used the multiphoton imaging flow cytometer to acquire 2000 FWM and SHG images of *C. zofingiensis* cells at 0–9 days after refreshing the culture medium for the cells and found from our analysis of the images that starch was distributed at the center of the cells at the early cell cycle stage and became delocalized at the later stage. Multiphoton imaging flow cytometry is expected to be an effective tool for statistical high-content studies of biological functions and optimizing the evolution of highly productive cell strains.

2 | RESULTS AND DISCUSSION

Figure 1 schematically shows the multiphoton imaging flow cytometer. Cells are injected into a microfluidic chip (SC-BU-300300-L, Translume) at a flow speed of 2 mm/s. Flowing cells pumped by a syringe pump are focused into a single stream by acoustic focusing with a piezoelectric transducer (2.44Z25*30R-SYX(C-213), Nihon Denkei Co., Ltd.). When each cell passes through a focused HeNe laser (HNL020LB, Thorlabs) beam spot, forward-scattered light of the HeNe laser beam is detected by an avalanche photodetector (APD120A/M, Thorlabs), which triggers image acquisition. Then, the cell flows through the FWM and SHG imaging region. The light source used for FWM and SHG imaging is a Ti:sapphire laser (Synegy, Spectra Physics) with a pulse width of 17 fs, a center wavelength of 793 nm, a spectral bandwidth of 43 nm, and a pulse repetition frequency of 75 MHz. The Ti:sapphire

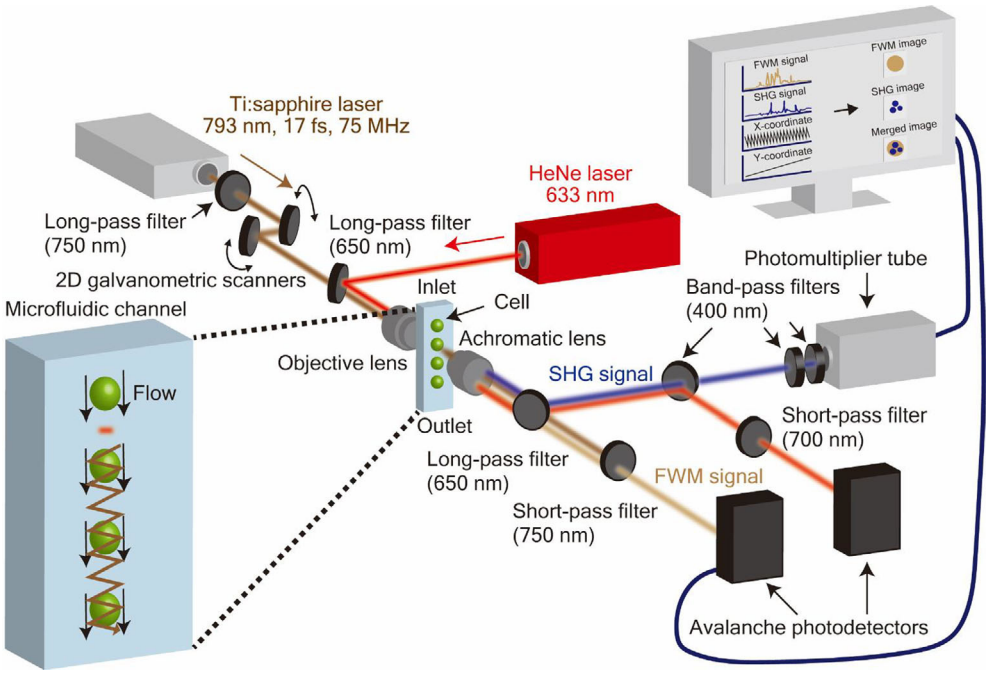

FIGURE 1 Schematic of the multiphoton imaging flow cytometer. Flowing cells pumped by a syringe pump are focused into a single stream by acoustic focusing with a piezoelectric transducer. When each cell passes through a focused HeNe laser beam spot, forward-scattered light of the HeNe laser beam is detected by an avalanche photodetector, which triggers image acquisition. Then, the cell flows through the FWM and SHG imaging region. Ti:sapphire laser beam is scanned in the focal plane by a pair of galvanometric scanners. A 750-nm long-pass filter and a 750-nm short-pass filter are placed before and after the microfluidic chip, respectively, for the selective detection of a blue-shifted FWM signal with another avalanche photodetector. Three 400-nm bandpass filters are placed in front of a photomultiplier tube to detect SHG signal selectively. [Color figure can be viewed at wileyonlinelibrary.com]

laser beam is scanned in the focal plane over an area of 50 µm (perpendicular to the flow direction) × 150 µm (along the flow direction) by a pair of galvanometric scanners (6210H, Cambridge Technology) driven by a triangular wave at 500 Hz and 5 Hz, respectively. A 750-nm long-pass filter (FELH0750, Thorlabs) and a 750-nm short-pass filter (FESH0750, Thorlabs) are placed before and after the microfluidic chip, respectively, for the selective detection of a blue-shifted FWM signal with another avalanche photodetector (APD120A/M, Thorlabs). Three 400-nm bandpass filters (FBH400-40, Thorlabs) are placed in front of a photomultiplier tube (H7732-01, Hamamatsu Photonics) to detect an SHG signal. The output signal from the photomultiplier tube is amplified by a wide bandwidth amplifier unit (C6438-01, Hamamatsu Photonics). The detected FWM and SHG signals are digitized by a 14-bit data acquisition board (ATS9440, AlazarTech) at a sampling rate of 1 MS/s. A transistor-transistor logic (TTL) signal is synchronized with one scan of the galvanometric scanner at 5-Hz while the output signal from a capacitive position sensor is used to monitor the position of the 500-Hz galvanometric scanner. This information is used to assign sampling points for a 2D Voronoi interpolation to generate FWM and SHG images in a uniform 2D grid. Consequently, the multiphoton imaging flow cytometer enables FWM and SHG imaging at a frame rate of 10 frames per second with a pixel resolution of 100 × 100 pixels and a pixel size of 500 nm.

Figure 2A,B shows typical reconstructed FWM and SHG images of *C. zofingiensis* cells, respectively (see Supporting Information for the reconstruction of FWM and SHG images). The FWM images visualize the morphological features of cells based on the third-order nonlinear optical susceptibility of molecules within the cells, while the SHG images primarily visualize the distribution of starch accumulated in the cells [33]. Figure 2C shows the merged images of Figure 2A,B, which help visualize the relative distribution of starch inside the cells. For comparison and validation, Figure 2D,E shows an FWM and SHG image of a 6.0-µm polystyrene bead, respectively. The FWM image shows the shape of the bead while the SHG image does not show the bead because polystyrene is a centrosymmetric material and is invisible to SHG imaging.

To demonstrate the utility of multiphoton imaging flow cytometry, we used it to characterize cultures of *C. zofingiensis* cells from day 0 to day 9 (after glucose feeding) with a 1-day interval with an image acquisition time of 100 ms and a laser power of 70 mW at the cells. We acquired 2000 FWM and SHG images of *C. zofingiensis* cells at throughputs of 4–5 eps. The acquired images were analyzed using *CellProfiler 4.1.3*. FWM images were used to recognize the morphological features of the cells and determine their size (Figure S2). Figure 3A shows violin plots of the cell area and indicates that the cells became larger after glucose feeding. The size of the cells reached its maximum around day 6 and then decreased until day 9. Figure 3B shows bright-field images of *C. zofingiensis* cells without glucose feeding as well as 3 days, 6 days, and 9 days after glucose feeding. It is evident from Figure 3B that the cell size was maximized at day 6, which is consistent with the results from the FWM images (Figure 3A). Figure 3C shows violin plots of the cell area calculated from bright-

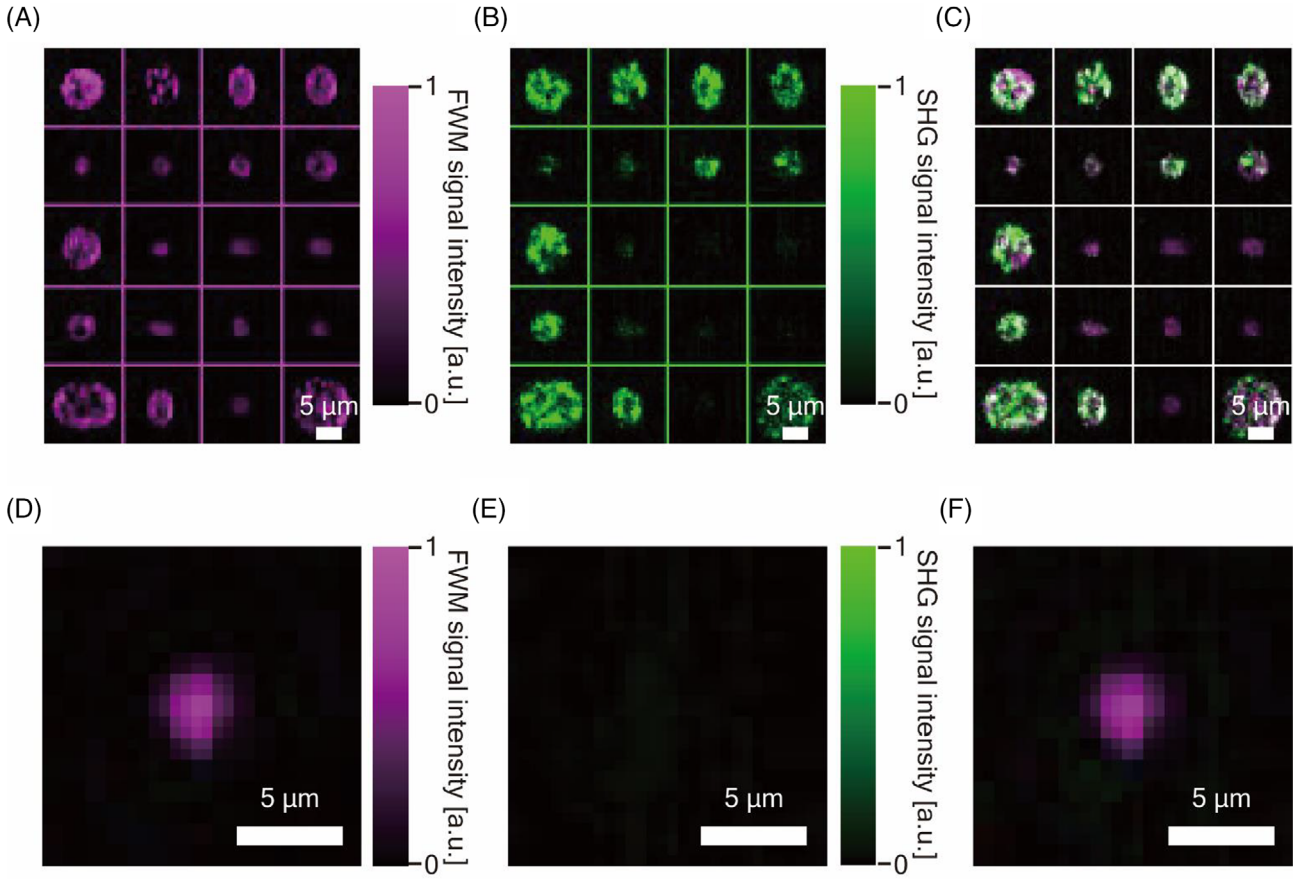

FIGURE 2 FWM and SHG images acquired by the multiphoton imaging flow cytometer. (A) Constructed FWM images of *C. zofingiensis* cells. (B) Constructed SHG images of *C. zofingiensis* cells. (C) Merged FWM and SHG images (Magenta: FWM images. Green: SHG images). (D) FWM image of a 6.0-μm polystyrene bead. (E) SHG image of the bead. (F) Merged FWM and SHG images (Magenta: FWM images. Green: SHG images) [Color figure can be viewed at wileyonlinelibrary.com]

field images (without Lugol staining; see Figure S3 for the bright-field image analysis). Although there exists a minor deviation between the average cell areas calculated from the FWM and bright-field images mainly due to the limited number of cells that were counted in bright-field imaging, the similar trends in the violin plots indicate that the FWM images are reliable for determining the cell area.

Figure 4A shows the violin plots of the integrated SHG signal intensity in the *C. zofingiensis* cells identified by the FWM images. The integrated single-cell SHG signal intensity was maximized on day 6. To confirm the origin of the SHG signals, we stained the cells with Lugol's solution (iodine-potassium iodide solution). Figure 4B shows the images of the Lugol-stained cells on days 0, 3, 6, and 9. Intracellular starch was visualized in blue-black due to the interaction of iodine in the Lugol reagent and starch [31]. It is evident from the images that the amount of accumulated starch evaluated based on the Lugol staining was also maximized at day 6, which matches the results obtained from the SHG images. For more quantitative analysis, we generated violin plots of the starch content from the bright-field images of the Lugol-stained cells (Figure 4C). Similarities in the distributions in Figure 4A,C indicate that the SHG images selectively probed starch molecules in the cells (see Figure S4 for analyzing the bright-field images of the Lugol-stained cells). The capability of visualizing intracellular non-centrosymmetric molecules by SHG imaging flow cytometry significantly broadens the application range of label-free imaging flow cytometry.

For a deeper understanding of morphogenesis in *C. zofingiensis* cells, we analyzed temporal changes in the spatial distribution of intracellular starch from the obtained images. Figure 5A shows scatter plots based on the fraction of the SHG signal intensity and the cell size. Here, the SHG intensity fraction was calculated by the module of "*MeasureObjectIntensityDistribution*" on *CellProfiler* 4.1.3. Each recognized cell was divided into two bins: bin 1 (inner) and bin 2 (outer). Then, the total SHG intensity inside each bin was calculated while the SHG intensity fraction in bin 1 was obtained (see Figure S5 for details about binning the cell). On days 0 and 1, the scatter plot is well accounted for by a single population, which is explained by recognizing that the cell cycle is highly uniform across the entire cell population immediately after the preculturing condition. After day 2, two populations emerged in each scatter plot, which correspond to mature cells and divided daughter cells. While the cell population with a larger cell size (>60 μm^2) shows a smaller SHG intensity fraction in bin 1 (i.e., starch is present more evenly in the cells), the cell population with a smaller cell size (<60 μm^2) shows a higher SHG intensity fraction (i.e., starch is present at the center of cells). Also, for the larger cell population (mature cells), an anti-correlation is evident between the cell size and the SHG fraction in bin

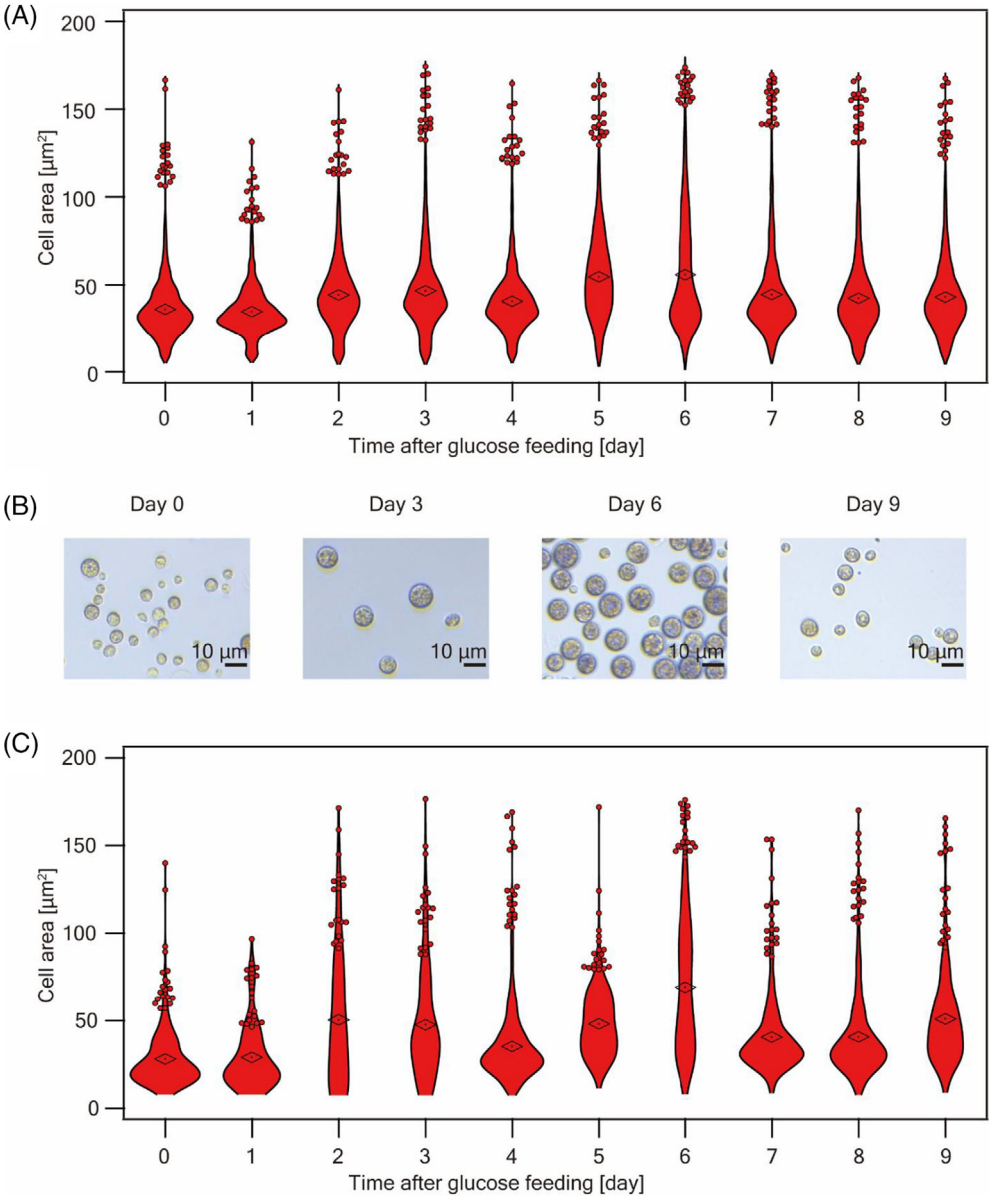

FIGURE 3 Evolution of the *C. zofingiensis* cell area after glucose feeding. (A) Violin plots of the cell area of *C. zofingiensis* cells calculated from FWM images. The dots on the plots represent mean cell area values. (B) Bright-field images of *C. zofingiensis* cells before glucose feeding and 3, 6, and 9 days after glucose feeding, respectively. (C) Violin plots of the cell area of *C. zofingiensis* cells calculated from bright-field images. The dots on the plots represent mean cell area values [Color figure can be viewed at wileyonlinelibrary.com]

1 (Figure 5). This anti-correlation is explained by the Fučíková et al. postulate that mature cells possess multiple parental chloroplasts, but younger cells have only a single chloroplast [34]. Another interesting finding is that the daughter cells' populations are shifted to a higher SHG fraction value on days 6 and 7, which indicates that starch was more localized at the center of the cells if they were divided on days 5 and 6. This result implies that starch accumulation in the daughter cells divided from the parental cells containing multiple [4, 8, 16, and] nuclei was more centered than those from less mature parental cells (2 nuclei) [35]. Conventional methods for studying cellular morphogenesis have been limited in conducting statistically significant analysis [36–39]. We think further research on statistical microbiological cellular dynamics by our label-free multiphoton imaging flow cytometer would lead to a more complete understanding of metabolism in *C. zofingiensis*, such as where and how interactions between photosynthesis in chloroplast and glucose metabolism in mitochondria take place [40].

3 | MATERIALS AND METHODS

3.1 | Multiphoton imaging

Our multiphoton imaging system employed a raster-scanned focused beam instead of line or light-sheet illumination schemes to increase the photon flux at the interrogation point for higher efficiency of nonlinear optical processes. We acquired SHG and FWM signals simultaneously from a sample by separating them using wavelength filters. In SHG, a portion of the incident light is frequency-doubled when it passes through non-centromeric materials. On the other hand, the FWM signal is detected as a broadened spectrum of the incident light when it passes through materials. In this work, we collected only the blue-shifted FWM signal as it was not influenced by the red-shifted autofluorescence from the sample.

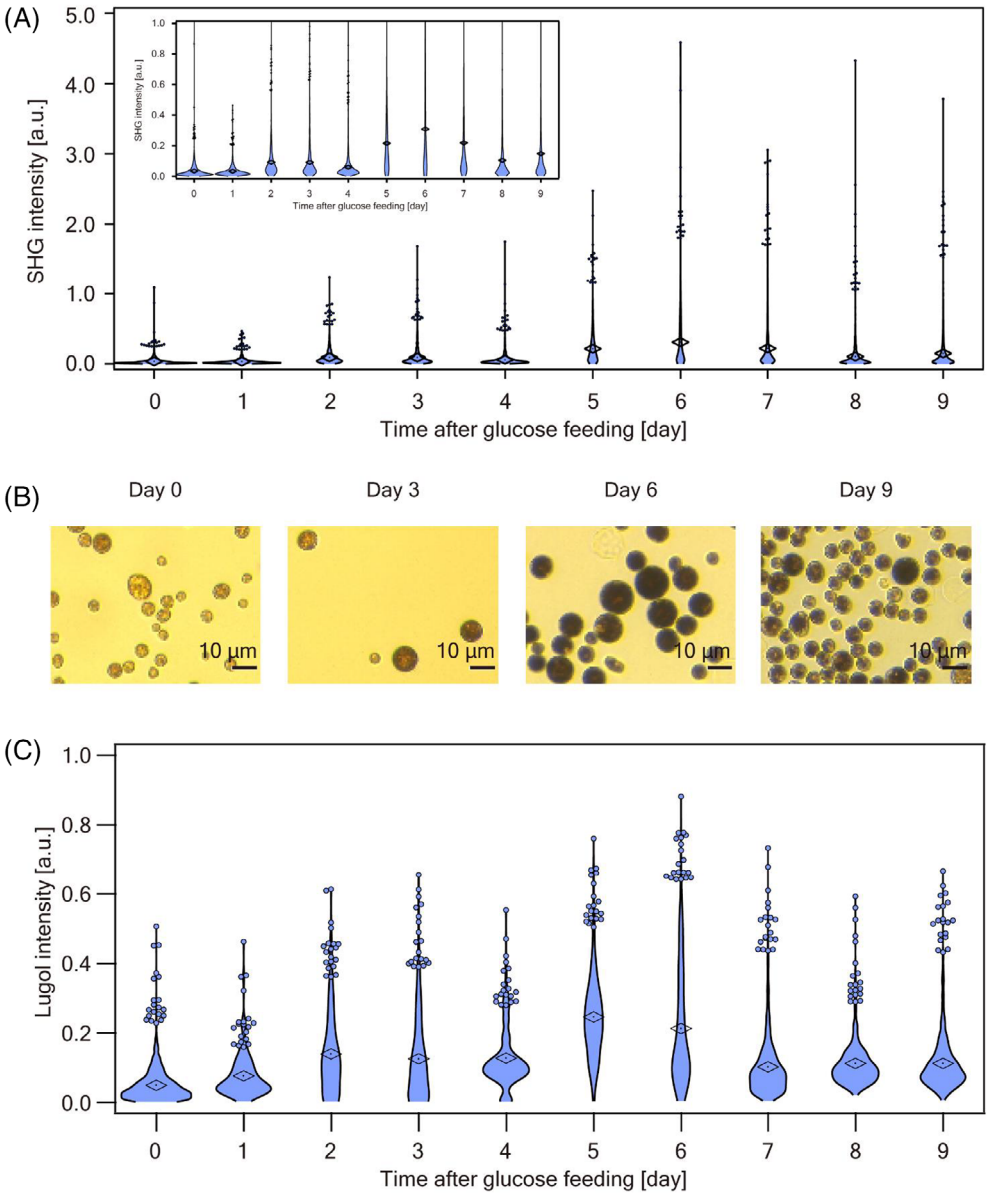

FIGURE 4 Evolution of the amount of starch in *C. zofingiensis* cells after glucose feeding. (A) Violin plots of integrated SHG signal intensity values from *C. zofingiensis* cells. The dots on the plots represent mean SHG signal intensity values. (B) Lugol-stained images of *C. zofingiensis* cells before glucose feeding and 3, 6, and 9 days after glucose feeding, respectively. (C) Violin plots of integrated Lugol intensity values from *C. zofingiensis* cells. The dots on the plots represent mean Lugol intensity values [Color figure can be viewed at wileyonlinelibrary.com]

3.2 | Microfluidic chip

We used a commercially available microfluidic chip (SC-BU-300300-L, Translume) for the multiphoton imaging flow cytometer. Flowing cells were focused into a single stream by acoustic focusing with a piezoelectric transducer (2.44Z25*30R-SYX(C-213), Nihon Denkei Co., Ltd.). We used a signal generator (DSG815, Rigor) and an amplifier (HSA4101, NF corporation) with an applied voltage of 7 V at a frequency of 2.62 MHz to generate resonance acoustic waves for acoustic focusing.

3.3 | Bootstrap analysis

We performed bootstrap analyses on the cell size measurements from FWM images, the total SHG intensity measurements from SHG images, the cell size measurements from bright-field images, and the Lugol intensity measurements from Lugol-stained images. Each bootstrap analysis was repeated with 2000 iterations. The results show that the standard deviations of the averaged values calculated from the bootstrap-resampled data are smaller than the day-by-day changes of the average values. These results support our claim that the time-dependent changes in cellular properties can be characterized by multiphoton imaging flow cytometry. See Supporting Information for the code we used and the numerical results of the bootstrap analyses.

3.4 | Sample preparation

C. zofingiensis (NIES2175) was provided by the Microbial Culture Collection at the National Institute for Environmental Studies (NIES;

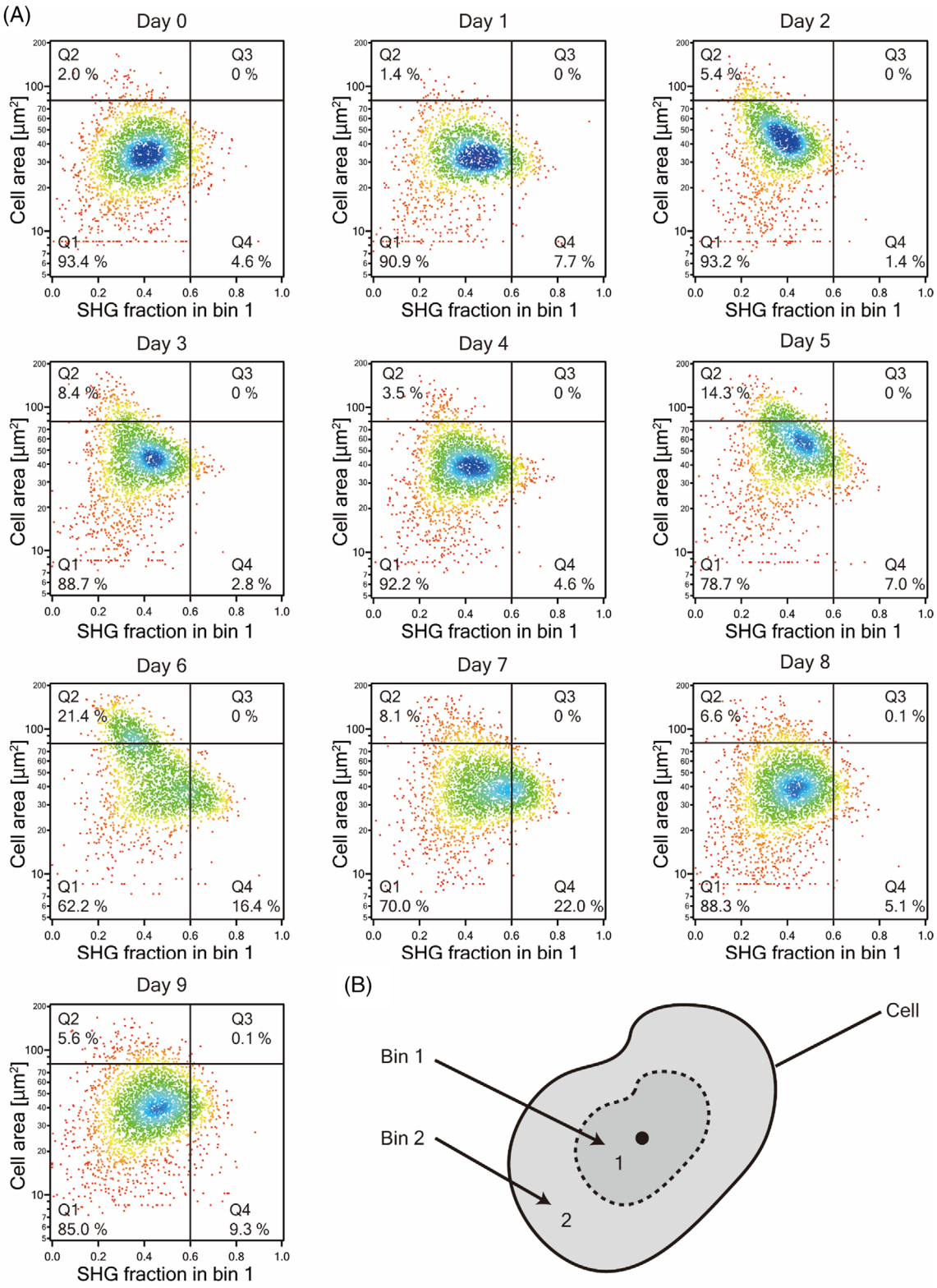

FIGURE 5 Evolution of the cell area versus SHG fraction in *C. zofingiensis* cells after glucose feeding. (A) Scatter plots of *C. zofingiensis* cells after glucose feeding, showing changes in the cell size and SHG intensity fraction in bin 1. (B) Binning schematic [Color figure can be viewed at wileyonlinelibrary.com]

Tsukuba, Ibaraki, Japan). The cells were precultured for 15 days in a modified acetate medium (mAC) [41]. After the preculture, glucose was added into the culture media such that the glucose concentration becomes 20 mg/mL, followed by further cultivation of the cells for 0–9 days. Throughout the entire cultivation process, the light condition was 14-h light/10-h dark cycle illumination (60 µmol/m^2/s for the

light condition) and the temperature in the incubator was maintained at 26°C. For multiphoton imaging flow cytometry experiments, the cell suspension was diluted to a concentration of 1.0×10^5 cells/mL with mAC medium. To prevent cell aggregation during the multiphoton imaging flow cytometry experiments, TWEEN 20 was added to a final concentration of 0.3% (volume/volume).

3.5 | Lugol staining

The standard Lugol staining procedure was employed for visualizing intracellular starch [31]. In a 1-mL suspension, the *C. zofingiensis* cells were fixed by treating them with 2.5% glutaraldehyde for 10 min, washed three times and stored in Dulbecco's phosphate-buffered saline (DPBS). The cells were stored at 4°C until the time of the Lugol staining experiment. Lugol [31] solution (5% of I_2/10% of KI) was added to the cells to a final concentration of 2% of I_2 and 4% of KI. The cells were incubated for 10 min and imaged using an optical microscope (Leica MC 170 HD, Leica microsystems) with a ×40 objective lens.

ACKNOWLEDGMENTS

This work was supported by JST PRESTO (JPMJPR1878), JST FOREST (JPMJFR216R), JSPS Gran-in-Aid for Scientific Research (B) (22H02029), JSPS Grant-in-Aid for Young Scientists (20K15227), JSPS Fellowship (19F19805), JSPS Core-to-Core Program, White Rock Foundation, and Research Foundation for Opto-Science and Technology.

CONFLICT OF INTEREST

K.G. is a shareholder of CYBO, Cupido, and LucasLand.

PEER REVIEW

The peer review history for this article is available at https://publons.com/publon/10.1002/cyto.a.24723.

ORCID

Julia Gala de Pablo https://orcid.org/0000-0003-0557-9632

Kotaro Hiramatsu https://orcid.org/0000-0003-0767-019X

REFERENCES

1. Lei C, Kobayashi H, Wu Y, Li M, Isozaki A, Yasumoto A, et al. High-throughput imaging flow cytometry by optofluidic time-stretch microscopy. Nat Protoc. 2018;13:1603–31.
2. Suzuki Y, Kobayashi K, Wakisaka Y, Deng D, Tanaka S, Huang CJ, et al. Label-free chemical imaging flow cytometry by high-speed multicolor stimulated Raman scattering. Proc Natl Acad Sci U S A. 2019;116:15842–8.
3. Işll Ç, De Haan K, Göröcs Z, Koydemir HC, Peterman S, Baum D, et al. Phenotypic analysis of microalgae populations using label-free imaging flow cytometry and deep learning. ACS Photonics. 2021;8:1232–42.
4. Lee KCM, Wang M, Cheah KSE, Chan GCF, So HKH, Wong KKY, et al. Quantitative phase imaging flow cytometry for ultra-large-scale single-cell biophysical phenotyping. Cytometry A. 2019;95:510–20.
5. Blasi T, Hennig H, Summers HD, Theis FJ, Cerveira J, Patterson JO, et al. Label-free cell cycle analysis for high-throughput imaging flow cytometry. Nat Commun. 2016;7:1–9.
6. Nitta N, Sugimura T, Isozaki A, Mikami H, Hiraki K, Sakuma S, et al. Intelligent image-activated cell sorting. Cell. 2018;175:266–76.
7. Rosendahl P, Plak K, Jacobi A, Kraeter M, Toepfner N, Otto O, et al. Real-time fluorescence and deformability cytometry. Nat Methods. 2018;15:355–8.
8. Isozaki A, Mikami H, Tezuka H, Matsumura H, Huang K, Akamine M, et al. Intelligent image-activated cell sorting 2.0. Lab Chip. 2020;20:2263–73.
9. Mikami H, Kawaguchi M, Huang CJ, Matsumura H, Sugimura T, Huang K, et al. Virtual-freezing fluorescence imaging flow cytometry. Nat Commun. 2020;11:1–11.
10. Mikami H, Lei C, Nitta N, Sugimura T, Ito T, Ozeki Y, et al. High-speed imaging meets single-cell. Analysis Chem. 2018;4:2278–300.
11. Doan M, Vorobjev I, Rees P, Filby A, Wolkenhauer O, Goldfeld AE, et al. Diagnostic potential of imaging flow cytometry. Trends Biotechnol. 2018;36:649–52.
12. Lee KCM, Guck J, Goda K, Tsia KK. Toward deep biophysical cytometry: prospects and challenges. Trends Biotechnol. 2021;39:1249–62.
13. Lau AKS, Shum HC, Wong KKY, Tsia KK. Optofluidic time-stretch imaging-an emerging tool for high-throughput imaging flow cytometry. Lab Chip. 2016;16:1743–56.
14. Yip GGK, Lo MCK, Yan W, Lee KCM, Lai QTK, Wong KKY, et al. Multimodal FACED imaging for large-scale single-cell morphological profiling. APL Photonics. 2021;6:070801.
15. Nitta N, Iino T, Isozaki A, Yamagishi M, Kitahama Y, Sakuma S, et al. Raman image-activated cell sorting. Nat Commun. 2020;11:1–16.
16. Gala De Pablo J, Lindley M, Hiramatsu K, Goda K. High-throughput raman flow cytometry and beyond. Acc Chem Res. 2021;54:2132–43.
17. Zong C, Premasiri R, Lin H, Huang Y, Zhang C, Yang C, et al. Plasmon-enhanced stimulated Raman scattering microscopy with single-molecule detection sensitivity. Nat Commun. 2019;10:1–11.
18. Mahou P, Olivier N, Labroille G, Duloquin L, Sintes J-M, Peyriéras N, et al. Combined third-harmonic generation and four-wave mixing microscopy of tissues and embryos. Biomed Opt Express. 2011;2:2837–49.
19. Wang Y, Lin C-Y, Nikolaenko A, Raghunathan V, Potma EO. Four-wave mixing microscopy of nanostructures. Adv Opt Photonics. 2011;3:1–52.
20. Nadiarnykh O, LaComb RB, Brewer MA, Campagnola PJ. Alterations of the extracellular matrix in ovarian cancer studied by second harmonic generation imaging microscopy. BMC Cancer. 2010;10:1–14.
21. Brackmann C, Bengtsson A, Alminger ML, Svanberg U, Enejder A. Visualization of β-carotene and starch granules in plant cells using CARS and SHG microscopy. Raman Spectrosc. 2011;42:586–92.
22. Sugiyama N, Sonay AY, Tussiwand R, Cohen BE, Pantazis P. Effective labeling of primary somatic stem cells with batio3 nanocrystals for second harmonic generation imaging. Small. 2018;14:1–9.
23. Collier BB, Awasthi S, Lieu DK, Chan JW. Non-linear optical flow cytometry using a scanned bessel beam light-sheet. Sci Rep. 2015;5:1–8.
24. Lin M, Liu Q, Liu C, Qiao X, Shao C, Su X. Label-free light-sheet microfluidic cytometry for the automatic identification of senescent cells. Biomed Opt Express. 2018;9:1692–703.
25. Kumar P, Joshi P, Basumatary J, Mondal PP. Light sheet based volume flow cytometry (VFC) for rapid volume reconstruction and parameter estimation on the go. Sci Rep. 2022;12:1–5.
26. Herbig M, Isozaki A, Carlo D, Guck J, Nitta N, Damoiseaux R, et al. Best practices for reporting throughput in biomedical research. Nat Methods. 2022;5:1–2.
27. Cinar SO, Chong ZK, Kucuker MA, Wieczorek N, Cengiz U, Kuchta K. Bioplastic production from microalgae: a review. Int J Environ Res Public Health. 2020;17:1–21.

28. Rumin J, Nicolau E, de Oliveira RG, Fuentes-Grünewald C, Picot L. Analysis of scientific research driving microalgae market opportunities in Europe. Mar Drugs. 2020;18:1–31.
29. Gifuni I, Olivieri G, Krauss IR, D'Errico G, Pollio A, Marzocchella A. Microalgae as new sources of starch: isolation and characterization of microalgal starch granules. Chem Eng Trans. 2017;57:1423–8.
30. Varfolomeev SD, Wasserman LA. Microalgae as source of biofuel, food, fodder, and medicines. Appl Biochem Microbiol. 2011;47:789–807.
31. Takeshita T, Takeda K, Ota S, Yamazaki T, Kawano S. A simple method for measuring the starch and lipid contents in the cell of microalgae. Cytologia (Tokyo). 2015;80:475–81.
32. Fernandes B, Dragone G, Abreu AP, Geada P, Teixeira J, Vicente A. Starch determination in Chlorella vulgaris-a comparison between acid and enzymatic methods. J Appl Psychol. 2012;24:1203–8.
33. Dragone G, Fernandes BD, Abreu AP, Vicente AA, Teixeira JA. Nutrient limitation as a strategy for increasing starch accumulation in microalgae. Appl Energy. 2011;88:3331–5.
34. Fučíková K, Lewis LA. Intersection of chlorella, Muriella and Bracteacoccus: resurrecting the genus Chromochloris Kol et Chodat (Chlorophyceae, Chlorophyta). Fottea (Praha). 2012;12:83–93.
35. Koren I, Boussiba S, Khozin-Goldberg I, Zarka A. Chromochloris zofingiensis (Chlorophyceae) divides by consecutive multiple fission cell-cycle under batch and continuous cultivation. Biology (Basel). 2021;10:1–17.
36. Liu J, Sun Z, Gerken H, Liu Z, Jiang Y, Chen F. Chlorella zofingiensis as an alternative microalgal producer of astaxanthin: biology and industrial potential. Mar Drugs. 2014;12:3487–515.
37. Ani Azaman SN, Nagao N, Yusoff FM, Tan SW, Yeap SK. A comparison of the morphological and biochemical characteristics of chlorella sorokiniana and chlorella zofingiensis cultured under photoautotrophic and mixotrophic conditions. PeerJ. 2017;5:e3473.
38. Zhang Z, Sun D, Zhang Y, Chen F. Glucose triggers cell structure changes and regulates astaxanthin biosynthesis in Chromochloris zofingiensis. Algal Res. 2019;39:101455.
39. Zhang Z, Sun D, Zhang Y, Chen F. Chloroplast morphogenesis in Chromochloris zofingiensis in the dark. Algal Res. 2020;45:101742.
40. Zhang Z, Sun D, Cheng KW, Chen F. Investigation of carbon and energy metabolic mechanism of mixotrophy in Chromochloris zofingiensis. Biotechnol Biofuels. 2021;14:1–16.
41. Nozaki H, Makoto M. Morphology and paedogamous sexual reproduction in Chlorogonium Capillatum sp. nov. (Volvocales, Chlorophyta). J Phycol. 1995;31:655–63.

SUPPORTING INFORMATION

Additional supporting information can be found online in the Supporting Information section at the end of this article.

How to cite this article: Kinegawa R, Gala de Pablo J, Wang Y, Hiramatsu K, Goda K. Label-free multiphoton imaging flow cytometry. Cytometry. 2023;103(7):584–92. https://doi.org/10.1002/cyto.a.24723